Wiley Online Library
Early View publication on www.wileyonlinelibrary.com
(issue and page numbers not yet assigned;
citable using Digital Object Identifier – **DOI**)

Laser Photonics Rev., 1700025 (2017) / **DOI** 10.1002/lpor.201700025

LASER & PHOTONICS REVIEWS

Abstract Holography is of great interest for both scientific research and industry applications, but it has always suffered from the strong dependence on wavelength and polarization of the incident light. Having revisited the Huygens–Fresnel principle, we propose a novel holography mechanism by elaborately choosing discrete point sources (PSs) and realize it experimentally by mimicking the radiated fields of these PSs through carefully designed photon-nanosieves. Removing the modulation dispersion usually existing in traditional and metasurface holograms, our hologram empowers the simultaneous operation throughout the ultraviolet, entire visible and near-infrared wavelength regions without polarization dependence. Due to the deep-subwavelength dimension of nanosieves, this robust hologram offers a large angle-of-view of 40°×40° and possesses a lensing effect under a spherical-wave illumination, which can work as a high-resolution, lens-less and distortion-free microprojector that displays a 260× magnified image. It might open an avenue to a high-tolerance holographic technique for electromagnetic and acoustic waves.

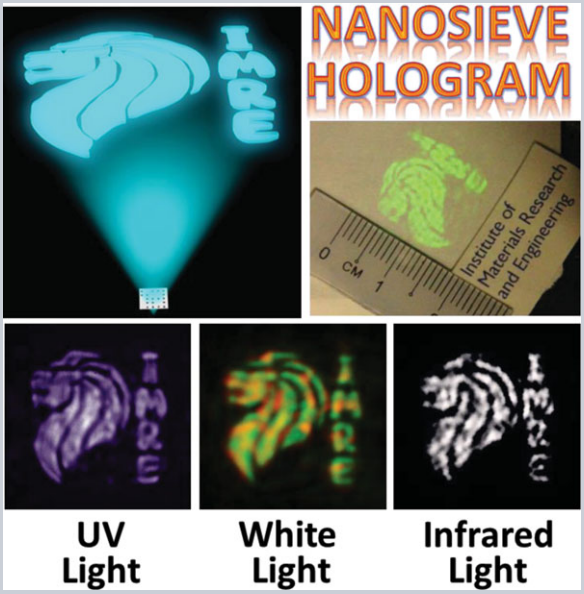

ORIGINAL PAPER

Photon-nanosieve for ultrabroadband and large-angle-of-view holograms

Kun Huang[1,], Hong Liu[1,**], Guangyuan Si[2,**], Qian Wang[1], Jiao Lin[2], and Jinghua Teng[1,*]**

1. Introduction

Optical holography has undergone substantial development for many applications since its invention in 1948 [1], such as X-ray imaging [2], optical manipulation [3], biological imaging [4], and data storage [5]. Among the holography family, computer-generated holography (CGH) has become the most intriguing member for its capability in reconstructing images of any real or virtual objects by using a pixelated phase [6] or amplitude [7–9] mask. However, traditional CGHs are not suitable for broadband operation because their modulated phase or amplitude has considerable dispersion [10–12]. For example, the phase-CGH in Fig. 1a obtains the phase modulation of $\varphi_\lambda = 2\pi(n–1)h/\lambda$, where n is the refractive index of medium at wavelength λ and h is the propagation distance of light through medium, by engineering h in the transparent medium like quartz [6, 13, 14] or tuning n in spatial light modulators [15, 16]. The phase modulation has a strong dependence on wavelength, named as modulation dispersion here, indicating such a CGH with serious modulation-induced aberration is only valid at the designed wavelength. Similarly, an amplitude-CGH also suffers from this modulation dispersion issue because the diffraction pattern (e.g., scale [17] and amplitude [7]) from a single unit is sensitive to the illuminating wavelength [18], which leads to the significant chromatic aberration and distortion in holographic images [10, 12]. Although novel designs [19] and cascaded holographic elements [11, 20] have been devoted to suppressing the chromatic dispersion, complete elimination of modulation dispersion is impossible due to these fundamental limitations of traditional CGHs.

Recently, metasurfaces [21, 22] consisting of gradually varied nanostructures have been demonstrated in controlling phase and amplitude [23] of a polarized light by plasmonic resonance in metals [21] or magnetic resonance in dielectrics [24–27]. These electromagnetic resonances are wavelength dependent, which determines that the phase or amplitude modulated by metasurfaces still has significant modulation dispersion (see Fig. 1b). As a result, metasurface CGHs for linear polarization usually operate at several discrete wavelengths [28–36]. In contrast, geometric metasurfaces allow broadband operation for a circularly polarized light due to the dispersion-less Pancharatnam–Berry phase [37]. Unfortunately, their amplitude responses are

[1] Institute of Materials Research and Engineering, Agency for Science, Technology and Research, 2 Fusionopolis Way, Innovis, #08-03, Singapore 138634, Singapore
[2] School of Engineering, RMIT University, Melbourne, Victoria 3001, Australia
**These authors contributed equally to this work
*Corresponding author: e-mail: jh-teng@imre.a-star.edu.sg

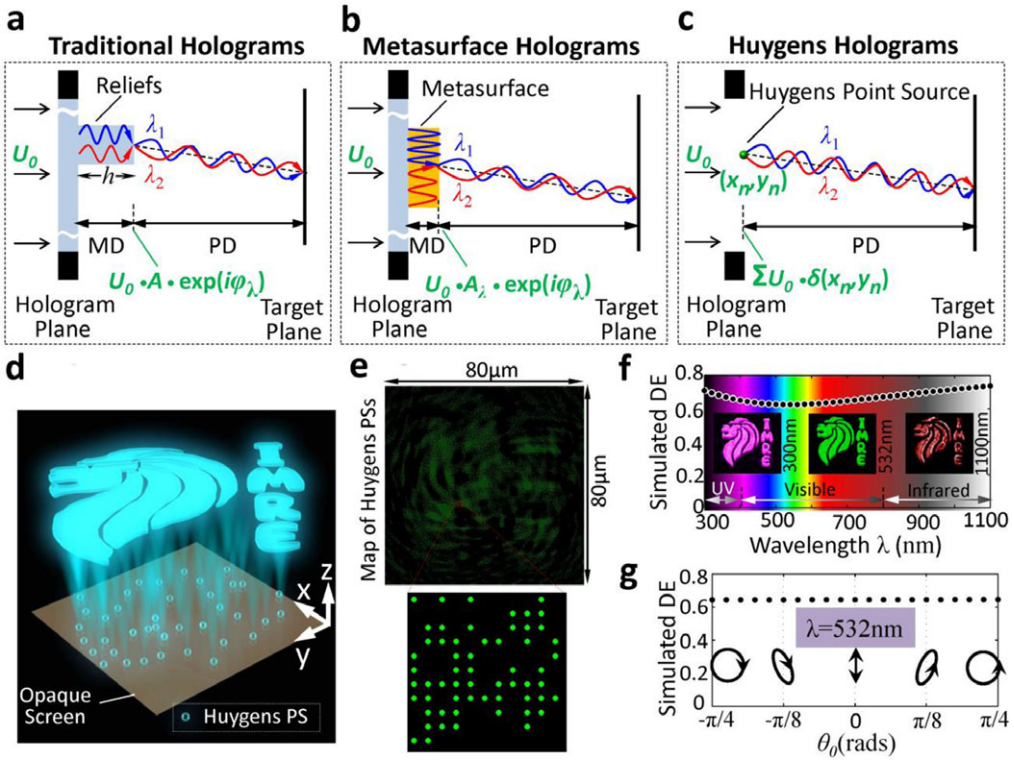

Figure 1 Principle of point-source-based holograms. (a) Traditional holograms based on the optical path-difference phase modulation of φ_λ with a strong dependence on wavelength. A chromatic modulation dispersion (MD) will be introduced immediately after the reliefs. (b) Metasurface holograms relying on electromagnetic resonances to achieve wavelength-dependent amplitude and phase modulation. (c) PS-based holograms using the emitting point sources without producing any MD. It has only the propagation dispersion that has little influence on the holographic image. (d) Sketch of PS-based holograms for displaying an image. (e) A map of PS-based hologram with 20, 931 PSs located in an 80 μm×80 μm square. Insert: A zoom-in view of a local region. The PSs are denoted by the green dots. (f) Simulated diffraction efficiency (DE) under the illumination of different wavelengths across the ultraviolet (UV), visible and near-infrared ranges. Inserts: The simulated intensity profiles at wavelengths of 300 nm, 532 nm and 1100 nm. (g) Simulated DE as a function of incident polarizations at the wavelength of 532 nm. The inserts (i.e., circles and arrow) show the states of polarization of incident light.

closely related to the wavelength of plasmonic or magnetic resonance so that their efficiency decreases rapidly when the illuminating wavelength falls out of a narrow resonance band [24, 38–41]. To the best of our knowledge, the largest ever reported bandwidth of geometric metasurface holograms is ~400 nm [39] in both theory and experiment. Furthermore, all these metasurface CGHs only work under either linear or circular polarization because the nanostructures respond selectively to the polarization of incident light [42]. In addition, the absorption of high-index dielectric materials makes them unsuitable for operation at shorter wavelengths such as the ultraviolet (UV) and blue ranges [24]. There is no solution among existing holographic techniques to simultaneously enable polarization-independent, distortion-free, large angle-of-view and ultrabroadband operation spanning from the UV to near-infrared (IR) wavelengths, which are highly desired for high-performance holography.

Here, we propose a holographic strategy of employing an array of point sources (PSs) to reconstruct the diffractive images without any additional phase or amplitude modulation and thus remove the intractable modulation dispersion for an ultrabroadband (>700 nm bandwidth) operation of light across the ultraviolet, visible and near-IR wavelength ranges. Realized experimentally by utilizing photon-nanosieves with 20 931 holes at an optimized diameter of 100 nm, this PSs hologram is verified to enable both ultrabroadband (from 355 nm to 1064 nm) and polarization-independent (i.e., linear, circular and elliptical polarizations) operations, meanwhile possess fascinating functionalities such as large angle-of-view under tilting plane-wave illumination and a distortion-free lensing effect under spherical-wave illumination.

2. Materials and methods

2.1. Design principle

The Huygens–Fresnel principle shows that diffraction of light by an aperture in an opaque screen could be described

by "a superposition of wavelets originating from an infinity of fictitious 'secondary' PSs located within the aperture" [43]. Its diffraction pattern is mainly dominated by the aperture shape because all the PSs within this aperture contribute to the interfered pattern. However, if only a finite number of discrete PSs are involved in the interference (Fig. 1c), the resulting pattern might be customized into any shape, e.g., a picture or hotspot, by carefully arranging the locations of these selected PSs, which implies a viable holography mechanism as sketched in Fig. 1d.

According to Rayleigh–Sommerfeld theory [43], the diffraction pattern of an array of PSs in Fig. 1d can be described as a superposition of electric fields from all these PSs

$$u(x, y, z) = \sum_{n=1}^{N} U_0(x_n, y_n) \cdot P(x, y, x_n, y_n, z, \lambda) \tag{1}$$

where $P = \frac{-1}{2\pi}\frac{\exp(ikR_n)}{R_n}(ik - \frac{1}{R_n})z$, $R_n{}^2 = (x_n - x)^2 + (y_n - y)^2 + z^2$, the incident electric field U_0 is taken as unity here for a plane wave, N is the total number of PSs, $k = 2\pi/\lambda$ and λ is the wavelength of light. Equation (1) contains two parts: the incident field $U_0(x_n, y_n)$ at the position (x_n, y_n) and the propagation kernel P. For a given N, the spatial position (x_n, y_n) of PSs in the opaque screen is the only variable but sufficient to achieve a customized pattern through careful optimization. It should be noted that $U_0(x_n, y_n)$ is not imprinted with any additional phase or amplitude modulation and therefore removes the intractable modulation dispersion physically, which is a significant difference from the previous holography mechanisms. Such a modulation-dispersion-free feature is at the cost of low optical efficiency because the filling factor of PSs cannot be large for reconstructing a hologram. Therefore, pursuing a high efficiency is beyond the scope of a Huygens hologram. It is worth noting that, although the modulation dispersion has been eliminated, the propagation kernel P describing the diffraction of a PS located at (x_n, y_n) provides the intrinsic propagation dispersion. This propagation dispersion cannot be eliminated in principle, however, it mainly influences the imaging position of a hologram and does not cause significant distortions or aberrations in the reconstructed holography image [24,38].

A genetic algorithm-based technique (see Supplementary Section 1 of Supporting Information) is employed here to determine the locations of PSs for reconstructing an image composed of the picture "Merlion" and letters "IMRE" (referring to Fig. 1d). Figure 1e shows the overall map of these optimized PSs with the smallest spacing of 250 nm, which is designed to reconstruct this image at $z_0 = 300\ \mu$m for the incident wavelength $\lambda_0 = 532$ nm. In Fig. 1f, we calculate the diffraction efficiency (DE), a ratio of the image intensity (target plane) to the total power of these PSs (hologram plane), that determines the signal-to-noise ratio (SNR = DE/(1–DE)) of a holographic image (not confused with the total efficiency that is defined as the ratio of image intensity to the total power of incident light). A large DE means a high-quality holographic image without any significant noise or background. The simulated DE is located between 62% and 73% with a smooth variation across a wide spectrum range of 300 nm to 1100 nm. The insets of Fig. 1g show the high-fidelity Merlion images simulated at three typical wavelengths of 300 nm, 532 nm, and 1100 nm, which theoretically manifest the robust, reliable and high-quality images across an ultrabroadband spectrum.

Its polarization response is investigated by using the vector Rayleigh–Sommerfeld theory [44]. Assuming that the PSs possess the same optical properties as incident light [43], all the PSs have the identical polarization profile of $\sin\theta_0\vec{\mathbf{e}}_x + i \cdot \cos\theta_0\vec{\mathbf{e}}_y$, where θ_0 determines the state of polarization. In its diffraction fields, only the dominated components $\vec{\mathbf{e}}_x$ and $\vec{\mathbf{e}}_y$ are considered in our calculations due to the negligible longitudinal component $\vec{\mathbf{e}}_z$ (Supplementary Section 2 and Supplementary Fig. S1 of Supporting Information) [35]. Figure 1g plots the calculated DEs as a function of θ_0 (their states of polarization are denoted by the insets), which shows a nearly constant of 64.3% without any dependence on linear, circular and elliptical polarizations.

2.2. Mimicking the electric fields of a point source by a nanohole

Some approaches have been proposed to approximate the Huygens PSs by the electrically small antennas at microwave and midinfrared frequencies [45–47], and dielectric nanodisks in the visible and near-infrared ranges [48]. However, they suffer from the strong wavelength dependence caused by the underlying electromagnetic resonances and the strong absorption of high-index materials, e.g. silicon, at shorter wavelength [42]. A small air hole is approximated frequently as a point source [49,50], especially when the distance between the hole and the target plane of interest is much larger than the hole diameter. A nanohole in an opaque screen cannot be taken as an ideal Huygens PS that requires a purely forward-propagating property without any reflection [46,47,51,52]. Nevertheless, we find that the radiated fields of an ideal PS are nearly identical to the optical fields diffracted from an air nanohole, which is critical because the reconstruction of a holography image mainly depends on the electric fields of a diffraction unit (such as a nanohole or PS) at the target plane. In addition, the transmitted wave from a nanohole propagates forwardly while the reflected light has no influence on the image reconstruction. More importantly, the air in a nanohole has the least absorption and dispersion for the spectral range from UV to near IR, which is not achievable by other approaches. Therefore, we adopt the concept of photon sieve [53] consisting of many nanoholes for realizing all the proposed advantages of our hologram.

The lateral profile of light from a nanohole perforated in an opaque screen has been investigated first, as sketched in Fig. 2a. Under the x-polarized illumination, the diffracting electric fields have a dominated E_x-component and an ignorable E_z-component under the

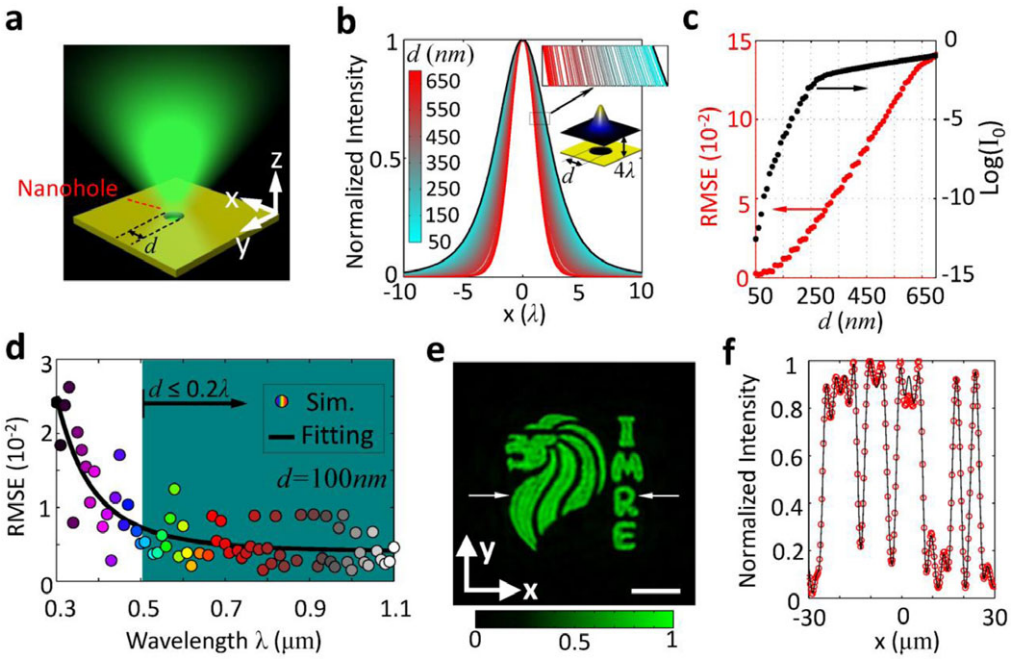

Figure 2 Mimicking a PS by a Nanohole. (a) Sketch for the radiation of a nanohole. The yellow part is the opaque screen made of PEC in our simulations. (b) Intensity profiles $I_{hole}(x, y = 0, z = 4\lambda)$ normalized by $I_0(x = 0, y = 0, z = 4\lambda)$ at a wavelength of 532 nm by using FDTD. The pseudocolors of curves stand for the diameter d of nanohole. The black curve is the normalized intensity profile $I_{ideal}(x, y = 0, z = 4\lambda)$ radiating from an ideal PS. (c) A quantitative evaluation of the radiation from a nanohole. The red dots are the RMSEs between $I_{hole}(x, y = 0, z = 4\lambda)$ (color curves in b) from a d-diameter nanohole and $I_{ideal}(x, y = 0, z = 4\lambda)$ (black curve in b) from an ideal PS. $RMSE = \sqrt{\sum_{n=1}^{N} [\, I_{hole}(x_n, 0, 4\lambda) - I_{ideal}(x_n, 0, 4\lambda)]^2/(N-1)}$, where N is the sampling number along x direction. The black dots show the logarithm of simulated $I_0 = I_{hole}(x = 0, y = 0, z = 4\lambda)$ in (b) for the holes with different diameters. (d) The broadband response of a 100-nm diameter nanohole for wavelengths from 300 nm to 1100 nm. It is characterized in terms of the RMSEs between $I_{hole}(x, y = 0, z = 4\lambda)$ and $I_{ideal}(x, y = 0, z = 4\lambda)$ by changing the illuminating wavelength λ. The color dots and solid curve are the simulated RMSEs and their corresponding fitting results, respectively. (e) Simulated image of nanosieve hologram by directly duplicating the locations of ideal PSs in Fig. 1e with 100-nm diameter nanoholes. Scale bar: 20 μm. (f) A comparison of line-scanning (i.e., the line between two white arrows in e) intensity profiles of the ideal (black curve) and nanosieve (red circles) hologram.

paraxial approximation. In Fig. 2b, we quantitatively investigated the lateral (i.e., x–y plane) intensity profiles at the z-cut plane of $z = 4\lambda$ ($\lambda = 532$ nm for example) by changing the hole diameter d from 50 nm to 700 nm. This distance is beyond the evanescent region, while it can facilitate an easy (i.e., lower demand on memory) implementation of the rigorously numerical simulation by using a finite-difference time-domain (FDTD, Lumerical Inc.) method, having a perfect electric-conductor screen with 200 nm thickness and a perfectly matched layer along all x-, y- and z-axes. Figure 2b shows that small nanoholes have nearly identical lateral intensity profiles to that of an ideal PS, which is verified by their small root-mean-square errors (RMSEs, see the red dots in Fig. 2c) between intensity profiles from a nanohole and an idea PS, e.g., $<5\times10^{-3}$ when $d<100$ nm. Small nanoholes lead to the low transmission of light as indicated by the rapidly decreasing on-axis intensity I_0 (black dots in Fig. 2c). Consequently, the 100-nm diameter nanohole is chosen here after a considerate balance between the optical performance and fabrication challenge of smaller nanoholes.

We have also checked its broadband operation in Fig. 2d, showing the acceptable RMSEs across the wavelengths from 300 nm to 1100 nm. The RMSE drops rapidly till around $\lambda = 500$ nm, after which it gradually converges to a small value of $\sim5\times10^{-3}$. This result suggests several important points in physics. First, the nanohole size can be reasonably set at a threshold of $d = 0.2\lambda$, below which nanoholes perform well to mimic the radiated electric fields of PSs without much deviation. Secondly, when $d<0.2\lambda$, there is no noticeable chromatic aberrations at the wavelength range of interest (e.g., from 0.5 μm to 1.1 μm in Fig. 2d), making the nanosieve hologram fundamentally outperform other binary amplitude holograms plagued by the strong chromatic aberrations [9, 10, 18]. Although the RMSEs increase rapidly at wavelengths smaller than 0.5 μm, the values are also kept at the level of $\sim10^{-2}$, which is still a reasonably good approximation of the radiated fields from

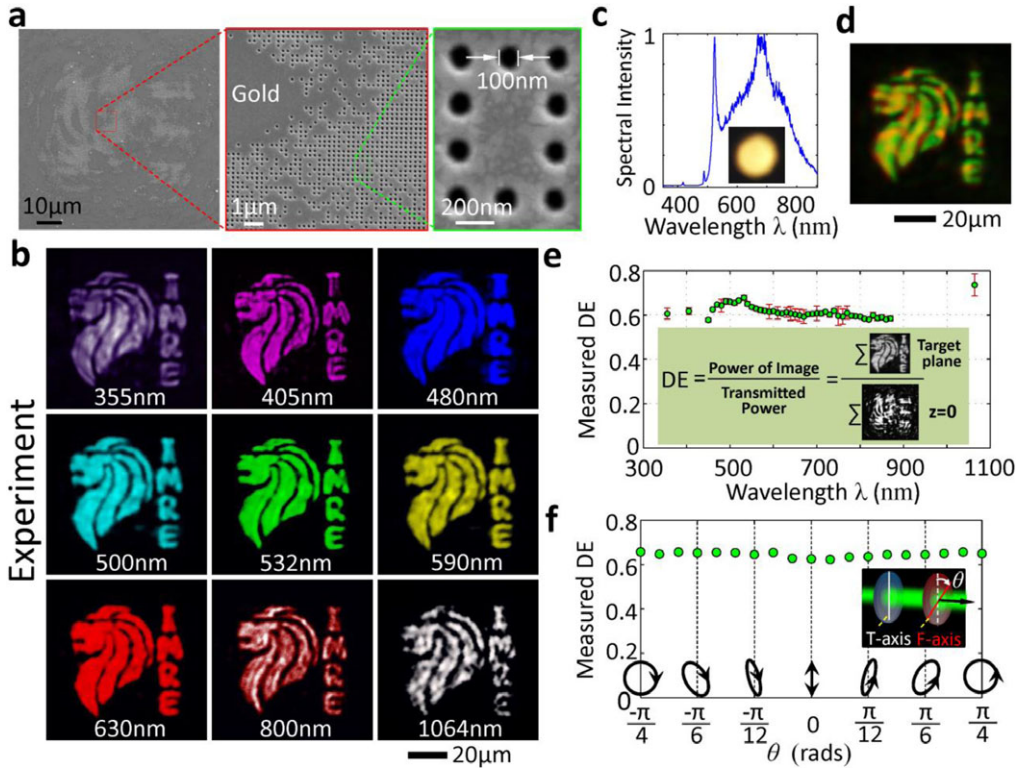

Figure 3 Experimental measurement of the photon-nanosieve hologram. (a) SEM images of fabricated photon-nanosieve sample in a gold film. (b) Measured holographic images at the selective wavelengths (distinguished by the pseudocolors) in different spectral ranges. (c) The measured spectrum of a white-light supercontinuum laser. Insert shows its intensity profile captured by a color CCD camera. (d) The captured holographic image under the illumination of white light in (c). (e) Measured DEs for different wavelengths. Insert: Definition of DE. The upper and lower images are captured by a CCD at the target and hologram ($z = 0$) planes, respectively. (f) Measured DEs for various incident polarizations that are realized experimentally by using a linear polarizer with its transmission axis (T-axis) denoted by the white line and a quarter waveplate with its fast-axis (F-axis) denoted by the red line, as shown in the inset.

a Huygens PS. The practical use of such a threshold is that the radiated fields of a nanoscale source with its diameter smaller than 0.2λ can be directly approximated by Eq. (1).

The 100-nm diameter nanohole is directly employed to substitute the PS of Fig. 1e and construct a photon-nanosieve hologram. To calculate its diffraction pattern, a powerful hybrid approach [35] is used instead of the FDTD technique that requires tremendous computing resources for such a hologram containing 20 931 nanoholes. Figure 2e displays the calculated image at the target plane while its line-scan intensity profile is provided by the red circles of Fig. 2f, which quantitatively matches well with that of the ideal hologram (black curve in Fig. 2f).

3. Results and discussions

3.1. Experimental verifications

To realize this photon-nanosieve hologram, we experimentally milled the 100-nm diameter nanohole array in a 200-nm thick gold film by using focused-ion beam (Helios Nanolab 600 DualBeam, FEI) with a milling current of 48 pA. Figure 3a shows the scanning electron microscope images of one fabricated sample, which has ~75.7% of nanoholes with their diameters located between 95 nm and 103 nm (Supplementary Section 3.1 and Supplementary Fig. S2 of Supporting Information). To verify their performances, a self-built experimental setup in a confocal configuration (Alpha 300S, WITec GmbH) is employed (Supplementary Section 3.2. and Supplementary Fig. S3(a) of Supporting Information) under the illumination of laser sources with various wavelengths from 355 nm to 1064 nm, respectively. Their intensity profiles are recorded by a charge-coupled-device (CCD) camera (CM-140GE-UV, JAI), as shown by the pseudocolor pictures in Fig. 3b. The high-fidelity images at those representative wavelengths verify that our photon-nanosieve hologram works well across the ultraviolet, entire visible and near-infrared ranges, with an operating bandwidth of >700 nm. Benefitting from the effectiveness of the photon-nanosieves, our hologram has no high-order diffraction and twin-image issues.

The broadband behavior is further characterized by a while-light source from a supercontinuum laser with its experimental spectrum and intensity profile shown in Fig. 3c. Figure 3d displays the resulting image with the intermixed green, yellow and red colors, recorded at $z_0 = 300\ \mu$m by a

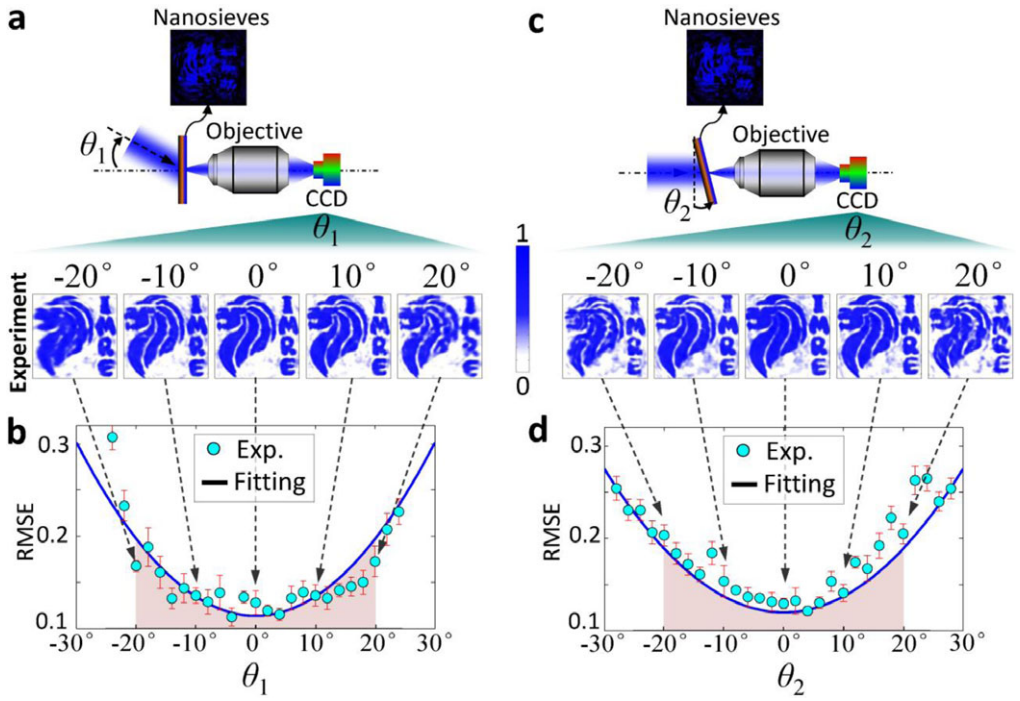

Figure 4 Incident angle tolerance. (a) Sketch of testing setup for tilting the incident light and the experimentally captured intensity profiles at different light incident angles θ_1. (b) RMSEs between captured and ideal images for the case in (a). The ideal image is the simulated image under the normal illumination with $\theta_1 = 0$. (c) Sketch of testing setup for tilting the hologram and the experimentally captured intensity profiles at different hologram tilting angles θ_2. (d) RMSEs between captured and ideal images for the case in (c). The ideal image is the simulated image under the normal illumination with $\theta_2 = 0$.

color CCD camera (AxioCam ICc3, Carl Zeiss). A captured video exhibiting the dynamic change of intensity profiles around $z = 300$ μm is also available in Supplementary Movie 1. Every holographic image for the involved wavelength λ is located at the different z-cut plane by following a simple relationship of $\lambda z = \lambda_0 z_0$ [24,38], see Supplementary Section 3.3 and Supplementary Fig. S4 of Supporting Information. Due to the chromatic dispersion caused by the small z-shift between two neighboring images, the overall image in Fig. 3d is colorful. However, its designed shape of "Merlion" and "IMRE" is well maintained without any distortion. This important feature makes our photon-nanosieve hologram competent at working as a white-light hologram.

The experimental DE is evaluated by the ratio of the intensity of captured holographic image (the upper image in the insert of Fig. 3e) to the transmitted power (the lower image) that is equivalent to the total power emitting from all PSs. Figure 3e shows the measured DE with a value of around 60% over a wide spectrum from 355 nm to 1064 nm, as predicted. Such high and stable DEs are essential to guarantee the high-quality images with minimum background noise. The polarization response is investigated by using a 532-nm laser for example. Referring to the inserts of Fig. 3f, the states of polarization (linear, circular and elliptical polarizations) of the incident beam could be tuned by manipulating a polarization converter composed of a linear polarizer and a quarter waveplate. The experimental DEs in Fig. 3f shows a nearly constant of 64.5% ($\pm$2%), indicating its independence on the incident polarizations. This can be attributed to the fact that the diffracting light directly inherits the incident-light polarization due to the axially symmetric geometry of a circular nanohole [54]. The low transmission of our nanohole makes the total efficiency (mainly constrained by the filling factor of holes and the transmission of a single hole) of our hologram below 1%. Potentially the transmission could be enhanced by increasing the hole size (see Fig. 2c) [54] but with some trade-offs on aberration (see Fig. 2b), or by using some active light-emitting nanocrystals [55–57] at the locations of holes.

3.2. Large angle-of-view

Our photon-nanosieve hologram also has superior tolerance to the incident angle of a tilting plane wave, verified by two experiments. First, we rotate the illuminating light to form a tilting angle of θ_1, as shown in Fig. 4a. The plane wave is approximated experimentally by a collimated Gaussian beam with a 488-nm wavelength as an example. As θ_1 changes, the captured image shifts its location in CCD, accompanied with a gradual variation in image quality. Five measured images are provided in the insets of Fig. 4a from $\theta_1 = -20°$ to $\theta_1 = 20°$ with an interval of 10° (see more images with an interval of 2° in Supplementary Fig. S5 of Supporting Information). Quantitatively, we

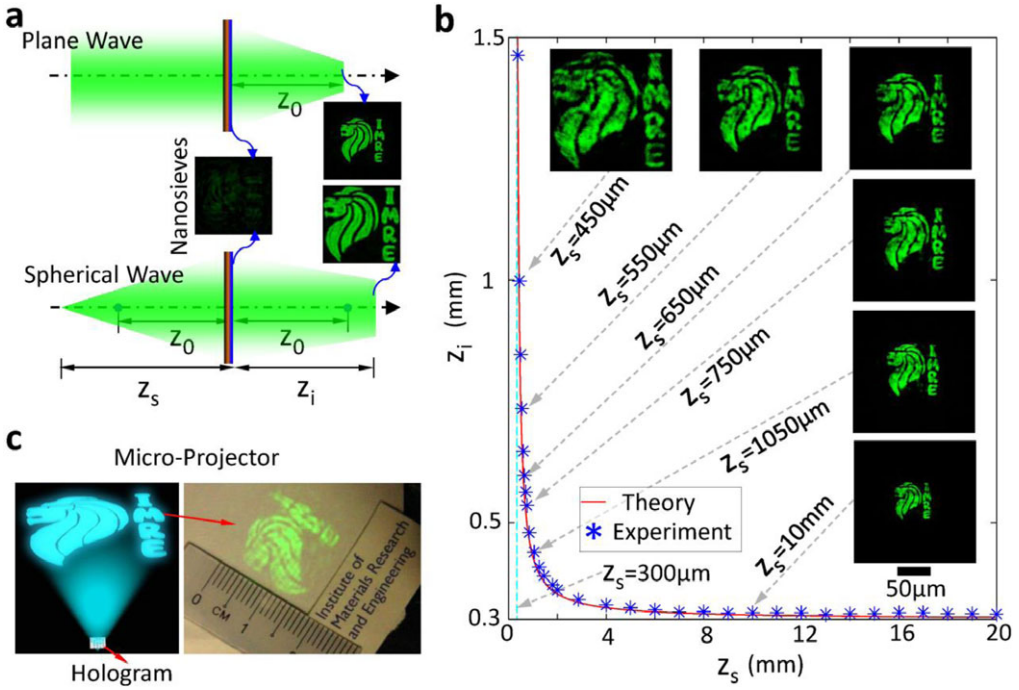

Figure 5 Lensing effect for magnified image projection. (a) Sketch for demonstrating the lensing effect. Under a plane-wave illumination, the photon-nanosieve hologram could generate a 58 μm×58 μm image at $z = z_0$. For a spherical-wave illumination, the same photon-nanosieve hologram is able to generate a magnified image at $z = z_i$. The center of sphere of this spherical wave is located at a distance of z_s from the hologram plane. (b) Theoretical (red curve) and measured (star) relationship between z_s and z_i. Inserts: Experimentally captured intensity profiles at different z_s. The scale bar is valid for all the images. (c) Working principle of a microprojector based on our photon-nanosieve hologram. Insert: Projected image with a magnification of ~260× captured by a single lens-reflex camera.

compare their RMSEs between the captured and ideal images in Fig. 4b, indicating an increasing deviation for large $|\theta_1|$. Since the maximal RMSEs is less than 20% within the range of $-20° \le \theta_1 \le 20°$, this hologram exhibits a high tolerance to incident angle of 40°×40°. Secondly, referring to Fig. 4c, we rotate the hologram to achieve a tilting angle θ_2 between its normal direction and the optical axis. The recoded images show the similar tendency that the quality becomes poorer as $|\theta_2|$ increases, while a maximum of RMSEs is <20% in the pink region of Fig. 4d. These results validate its good tolerance to the tilting illumination, implying the nontrivial advantage over those holograms that only operate at normal incidence of light [16, 36, 38–40]. Physically, the large angle-of-view is benefitted from the deep-subwavelength size of holes in our hologram.

3.3. Lensing effect

This high angle-tolerance enables our photon-nanosieve hologram to exhibit an intriguing lensing effect for holographic display. This phenomenon is demonstrated under the illumination of a spherical wave, which can be decomposed into a weighted superposition of many tilting plane waves according to the Fourier optics [43]. For an incident spherical wave having a distance of z_s between its center of sphere and hologram plane (see Fig. 5a), its electric field at the hologram plane is $U_0(x_n, y_n) = \exp(ikR_s)/R_s$, which $R_s^2 = x_n^2 + y_n^2 + z_s^2$. After substituting it into Eq. (1) and applying the paraxial approximation, one can find the imaging equation of a lens

$$\frac{1}{z_0} = \frac{1}{z_s} + \frac{1}{z_i} \tag{2}$$

and its magnification

$$M = \frac{z_i}{z_0} = \frac{1}{1 - z_0/z_s} \tag{3}$$

where z_i is the distance between the image plane and hologram plane. The detailed mathematical derivations can be found in Supplementary Section 4 of Supporting Information.

To verify this scenario experimentally, we implement the measurement (see Supplementary Fig. S3b of Supporting Information) by taking the 532-nm wavelength spherical-wave illumination for example. Figure 5b shows the measured z_s and z_i, which is consistent with the prediction by Eq. (2). The magnification of image can be observed especially when z_s approaches $z_0 = 300$ μm. During this process, the spherical wave incident on the hologram area contains more large tilting angle plane-wave components, whose largest angle is $\theta = 10.6°$ (i.e., $\tan^{-1}(40\sqrt{2}/300)$). Fortunately, it is still below the operating limitation of

$|\theta| = 20°$for our photon-nanosieve hologram, without producing any pincushion or barrel distortion [58].

Such a lensing functionality suggests an immediate application of our photon-nanosieve hologram working as a lens-less lightweight microprojector for portable display. In Fig. 5c, a proof-of-concept Merlion image with ~15 mm×15 mm size is experimentally obtained by carefully tuning z_s (see Supplementary Fig. S3c of Supporting Information). It should be emphasized that this image is directly projected onto a screen, without any optical component between this screen and the hologram plane, and captured by a simple family-used single-lens-reflex camera. Since the dimension of the designed image is ~58 μm×58 μm, a magnification of ~260 has been achieved without any distortion, which is usually suppressed with the help of a complex lens group in commercial projectors. No bulky lenses are needed here to correct the aberration so that it reduces the cost in optical design and the size of the whole system. The chip size of our microprojector is greatly scaled down to 80 μm×80 μm, which is ~10^{-4} of a commercial liquid crystal chip (~0.78 inch×0.49 inch, EPSON EB-536Wi Short Throw Projector). The much smaller pixel pitch of 250 nm (compared with ~15.5 μm in a liquid crystal pixel) renders a higher resolution. These features make this photon-nanosieve hologram a fascinating platform for portable displays, although its reconfigurability may need to resort to other technologies [59, 60].

4. Conclusions and outlook

In summary, a photon-nanosieve hologram is proposed and studied comprehensively. Nanoholes are used as practical point sources with an evaluation methodology provided. This technique opens up several unexploited areas in holography research and significantly relieves the rigorous limitations about the operating environment. The demonstrated hologram can operate simultaneously with polarization independence, distortion-free, high resolution and ultrabroadband from UV to near-IR. Furthermore, the large angle-of-view, lensing functionality and compact volume of the nanophoton-sieve holograms promise a plethora of potential applications in portable holographic display and virtual reality. Last but not least, the point-source-based Rayleigh–Sommerfeld theory has set a versatile platform for modeling optical field of other point-like nanoemitters such as nanocrystals.

Supporting Information

Additional supporting information may be found in the online version of this article at the publisher's website.

Acknowledgements. We thank Dr. Yanjun Liu and Dr. Andrew C. Y. Ngo for their valuable suggestions and appreciate H. K. Hui and S. L. Teo for their help in nanofabrication. The work was financially supported by the Institute of Materials Research and Engineering (IMRE/15-2C0308) and the Agency for Science, Technology and Research (Grant No. 152 148 0031).

Author Contributions K.H. developed the theory and carried out the hologram design and optimization. H.L. and G.S. prepared the samples. G.S., K.H., Q.W. and J.L. fabricated the samples. K.H., H.L. and J.T. implemented the experimental characterization and measurement. K.H., H.L., J.L. and J.T. wrote the manuscript. J.T. initiated the photon-nanosieve work and supervised the project. All authors analyzed the data and discussed the results.

Received: 26 January 2017, **Revised:** 8 March 2017,
Accepted: 22 March 2017

Published online: 10 April 2017

References

[1] D. Gabor, Nature **16**, 777–778 (1948).
[2] S. Eisebitt, J. Lüning, W. F. Schlotter, M. Lörgen, O. Hellwig, W. Eberhardt, and J. Stöhr, Nature **432**, 885–888 (2004).
[3] J. E. Curtis, B. A. Koss, and D. G. Grier, Opt. Commun. **207**, 169–175 (2002).
[4] P. Marquet, B. Rappaz, P. J. Magistretti, E. Cuche, Y. Emery, T. Colomb, and C. Depeursinge, Opt. Lett. **30**, 468–470 (2005).
[5] J. F. Heanue, M. C. Bashaw, and L. Hesselink, Volume holographic storage and retrieval of digital data. Science **265**, 749–752 (1994).
[6] L. Lesem, P. Hirsch, and J. Jordan, IBM J. Res., and Dev. **13**, 150–155 (1969).
[7] B. R. Brown and A. W. Lohmann, Appl. Opt. **5**, 967–969 (1966).
[8] E. N. Leith and J. Upatnieks, J. Opt. Soc. Am. **52**, 1123–1128 (1962).
[9] A. W. Lohmann and D. P. Paris, Appl. Opt. **6**, 1739–1748 (1967).
[10] J. N. Latta, Appl. Opt. **10**, 609–618 (1971).
[11] J. N. Latta, Appl. Opt. **11**, 1686–1696 (1972).
[12] S. J. Bennett, Appl. Opt. **15**, 542–545 (1976).
[13] J. Turunen, A. Vasara, and J. Westerholm, Opt. Eng. **28**, 281162 (1989).
[14] R. Bartolini, Appl. Opt. **13**, 129–139 (1974).
[15] F. Mok, J. Diep, H. Liu, and D. Psaltis, Opt. Lett. **11**, 748–750 (1986).
[16] K. Huang, H. Gao, G. Cao, P. Shi, X. Zhang, and Y. Li, Appl. Opt. **51**, 5149–5153 (2012).
[17] M. W. Farn, M. B. Stern, W. B. Veldkamp, and S. Medeiros, Opt. Lett. **18**, 1214–1216 (1993).
[18] Y. Ichioka, M. Izumi, and T. Suzuki, Appl. Opt. **10**, 403–411 (1971).
[19] M. Assenheimer, Y. Amitai, and A. A. Friesem, Appl. Opt. **27**, 4747–4752 (1988).
[20] I. Weingärtner and K. J. Rosenbruch, J. Mod. Opt. **29**, 519–529 (1982).
[21] N. Yu, P. Genevet, M. A. Kats, F. Aieta, J. Tetienne, F. Capasso, and Z. Gaburro, Science **334**, 333–337 (2011).
[22] P. Genevet, D. Wintz, A. Ambrosio, A. She, R. Blanchard, and F. Capasso, Nature Nano. **10**, 804–809 (2015).

[23] L. Liu, X. Zhang, M. Kenney, X. Su, N. Xu, C. Ouyang, Y. Shi, J. Han, W. Zhang, and S. Zhang, Adv. Mater. **26**, 5031–5036 (2014).
[24] K. Huang, Z. Dong, S. Mei, L. Zhang, Y. Liu, H. Liu, H. Zhu, J. Teng, B. Luk'yanchuk, J. K.W. Yang, and C. Qiu, Laser Photon. Rev. **10**, 500–509 (2016).
[25] I. Staude, A. E. Miroshnichenko, M. Decker, N. T. Fofang, S. Liu, E. Gonzales, J. Dominguez, T. S. Luk, D. N. Neshev, I. Brener, and Y. Kivshar, ACS Nano **7**, 7824–7832 (2013).
[26] Y. Yu, A. Y. Zhu, R. Paniagua–Domínguez, Y. H. Fu, B. Luk'yanchuk, and A. I. Kuznetsov, Laser Photon. Rev. **9**, 412–418 (2015).
[27] A. Arbabi, Y. Horie, M. Bagheri, and A. Faraon, Nature Nano. **10**, 937–943 (2015).
[28] H. Butt, Y. Montelongo, T. Butler, R. Rajesekharan, Q. Dai, S. G. Shiva-Reddy, T. D. Wilkinson, and G. A. J. Amaratunga, Adv. Mater. **24**, OP331–OP336 (2012).
[29] Y. Montelongo, J. Tenorio-Pearl, W. Milne, and T. Wilkinson, Nano Lett. **14**, 294–298 (2013).
[30] Y. Montelongo, J. Tenorio-Pearl, C. Williams, S. Zhang, W. Milne, and D. Wilkinson, Proc. Natl. Acad. Sci. **111**, 12679–12683 (2014).
[31] Y. Huang, W. Chen, W. Tsai, P. Wu, C. Wang, G. Sun, and D. P. Tsai, Nano Lett. **15**, 3122–3127 (2015).
[32] Y. Yifat, M. Eitan, Z. Iluz, Y. Hanein, A. Boag, and J. Scheuer, Nano Lett. **14**, 2485–2490 (2014).
[33] B. Walther, C. Helgert, C. Rockstuhl, F. Setzpfandt, F. Eilenberger, E. Kley, F. Lederer, A. Tunnermann, and T. Pertsch, Adv. Mater. **24**, 6300–6304 (2012).
[34] F. Zhou, Y. Liu, and W. Cai, Opt. Express **21**, 4348–4354 (2013).
[35] K. Huang, H. Liu, F. J. Garcia-Vidal, M. Hong, B. Luk'yanchuk, J. Teng, and C. Qiu, Nature Commun. **6**, 7059 (2015).
[36] X. Ni, A. V. Kildishev, and V. M. Shalaev, Nature Commun. **4**, 2807 (2013).
[37] L. Huang, X. Chen, H. Mühlenbernd, G. Li, B. Bai, Q. Tan, G. Jin, T. Zentgraf, and S. Zhang, Nano Lett. **12**, 5750–5755 (2012).
[38] L. Huang, X. Chen, H. Muhlenbernd, H. Zhang, S. Chen, B. Bai, Q. Tan, G. Jin, K. Cheah, C. Qiu, J. Li, T. Zentgraf, and S. Zhang, Nature Commun. **4**, 2808 (2013).
[39] G. Zheng, H. Muhlenbernd, M. Kenney, G. Li, T. Zentgraf, and S. Zhang, Nature Nano. **10**, 308–312 (2015).
[40] D. Wen, F. Yue, G. Li, G. Zheng, K. Chan, S. Chen, M. Chen, K. Li, P. Wong, K. Cheah, E. Pun, S. Zhang, and X. Chen, Nature Commun. **6**, 8241 (2015).
[41] L. Huang, H. Muhlenbernd, X. Li, X. Song, B. Bai, Y. Wang, and T. Zentgraf, Adv. Mater. **27**, 6444–6449 (2015).
[42] L. Zhang, S. T. Mei, K. Huang, and C. Qiu, Adv. Opt. Mater. **4**, 818–833 (2016).
[43] J. W. Goodman, Introduction to Fourier Optics (Roberts and Company Publishers, 2005).
[44] H. Ye, C. Qiu, K. Huang, J. Teng, B. Luk'yanchuk, and S. P. Yeo, Laser Phys. Lett. **10**, 065004 (2013).
[45] F. Monticone, N. M. Estakhri, and A. Alù, Phys. Rev. Lett. **110**, 203903 (2013).
[46] C. Pfeiffer and A. Grbic, Phys. Rev. Lett. **110**, 197401 (2013).
[47] P. Jin and R.W. Ziolkowski, IEEE Trans. Antennas Wireless Propag. Lett. **9**, 501 (2010).
[48] M. Decker, I. Staude, M. Falkner, J. Dominguez, D. Neshev, I. Brener, T. Pertsch, and Y. Kivshar, Adv. Opt. Mater. **3**, 813–820 (2015).
[49] J. A. Romero and L. Hernández, J. Opt. Soc. Am. A **24**, 1071–1073 (2007).
[50] J. D. Jackson, Classical Electrodynamics (Wiley, 1999).
[51] A. E. H. Love, Philos. Trans. R. Soc. London **197**, 1 (1901).
[52] J. M. Geffrin, B. Garcia-Camara, R. Gomez-Medina, P. Albella, L. S. Froufe-Perez, C. Eyraud, A. Litman, R. Vaillon, F. Gonzalez, M. Nieto-Vesperinas, J. J. Saenz, and F. Moreno, Nature Commun. **3**, 1171 (2012).
[53] L. Kipp, M. Skibowski, R. L. Johnson, R. Berndt, R. Adelung, S. Harm, and R. Seemann, Nature **414**, 184–188 (2001).
[54] F. J. Garcia-Vidal, L. Martin-Moreno, T. W. Ebbesen, and L. Kuipers, Rev. Mod. Phys. **82**, 729–787 (2010).
[55] W. K. Leutwyler, S. L. Bürgi, and H. Burgl, Science **271**, 933–937 (1996).
[56] V. I. Klimov, A. A. Mikhailovsky, S. Xu, A. Malko, J. A. Hollingsworth, C. A. Leatherdale, H. J. Eisler, and M. G. Bawendi, Science **290**, 314–317 (2000).
[57] M. Achermann, M. A. Petruska, S. Kos, D. L. Smith, D. D. Koleske, and V. I. Klimov, Nature **429**, 642–646 (2004).
[58] M. Born and E. Wolf, Principles of Optics (CUP Archive, 2000).
[59] G. Wang, X. Chen, S. Liu, C. Wong, and S. Chu, ACS Nano **10**, 1788–1794 (2016).
[60] Q. Wang, E. T. F. Rogers, B. Gholipour, C. Wang, G. Yuan, J. Teng, and N. I. Zheludev, Nature Photon. **10**, 60–65 (2016).